

GALEX FUV Observations of Comet C/2004 Q2 (Machholz): The Ionization Lifetime of Carbon

Jeffrey P. Morgenthaler

Planetary Science Institute, 1700 E. Fort Lowell, Ste 106, Tucson, AZ 85719, USA

`jpmorgen@psi.edu`

Walter M. Harris

Department of Applied Sciences, University of California at Davis, One Shields Ave., Davis, CA 95616, USA

Michael R. Combi

Department of Atmospheric, Oceanic and Space Sciences, The University of Michigan, 2455 Hayward St. Ann Arbor, MI 48109, Ann Arbor, MI, USA

Paul D. Feldman

*Department of Physics and Astronomy, The Johns Hopkins University
Charles and 34th Streets, Baltimore, Maryland 21218, USA*

Harold A. Weaver

Space Department, Johns Hopkins University Applied Physics Laboratory, 11100 Johns Hopkins Road, Laurel, MD 20723-6099, USA

ABSTRACT

We present a measurement of the lifetime of ground state atomic carbon, C(³P), against ionization processes in interplanetary space and compare it to the lifetime expected from the dominant physical processes likely to occur in this medium. Our measurement is based on analysis of a far ultraviolet (FUV) image of comet C/2004 Q2 (Machholz) recorded by the *Galaxy Evolution Explorer* (GALEX) on 2005 March 1. The bright C I 1561 Å and 1657 Å multiplets dominate the GALEX FUV band. We used the image to create high signal-to-noise ratio radial profiles that extended beyond 1×10^6 km from the comet nucleus. Our measurements yielded a total carbon lifetime of $7.1 - 9.6 \times 10^5$ s (ionization rate of $1.0 - 1.4 \times 10^{-6} \text{ s}^{-1}$) when scaled to 1 AU. This compares favorably to calculations assuming solar photoionization, solar wind proton change exchange and solar wind electron impact ionization are the dominant processes

occurring in this medium and that comet Machholz was embedded in the slow solar wind. The shape of the C I profiles inside 3×10^5 km suggests that either the CO lifetime is shorter than previously thought and/or a shorter-lived carbon-bearing parent molecule, such as CH_4 is providing the majority of the carbon in this region of the coma of comet Machholz.

Subject headings: atomic data – atomic processes – comets: individual (C/2004 Q2 (Machholz)) – interplanetary medium – methods: data analysis – molecular data – molecular processes – planets and satellites: auroræ – Sun: solar wind

1. Introduction

The volatile content of comets makes their compositional study via remote sensing particularly interesting and effective. Dozens of molecules and their elemental constituents have been detected in cometary coma and ion tail emissions (see e.g., Bockelée-Morvan et al. 2004; Feldman et al. 2004). Determining cometary nuclear composition from these remote sensing studies requires detailed understanding of the physical processes that govern coma and ion tail emissions. The study we report on here concerns one of these physical processes: the ionization of ground state atomic carbon, $\text{C}(^3\text{P})$.

UV emission from atomic carbon in comets was first detected in sounding rocket observations of comet C/1973 E1 (Kohoutek; Feldman et al. 1974; Opal et al. 1974). The emission consists of resonant fluorescence from $\text{C}(^3\text{P})$, with multiplets at 1561 Å and 1657 Å (see e.g., Figure 2 of Festou 1984 or Figure 1 of Tozzi et al. 1998). These emissions are extremely extended spatially (e.g., Figure 1 of McPhate et al. 1999), implying a very long lifetime of C I against ionization processes. The distribution of the C I emission rules out a direct nuclear source. For most comets, CO and CO_2 carry the bulk of carbon into cometary comæ (e.g., Table 1 of Bockelée-Morvan et al. 2004). CH_4 , C_2H_2 , C_2H_6 , CH_3OH , and H_2CO also contribute. As we discuss in detail in §4, the final radial velocity of a carbon atom liberated from any of these molecules is $\sim 4 \text{ km s}^{-1}$. The lifetimes of the parent molecules are long enough to place the liberated carbon well beyond the collision sphere of any comet observed in the modern era. Thus, the average carbon atom released from a typical comet becomes an excellent test particle to probe conditions in interplanetary space unperturbed by the presence of the comet or any other solar system body. By observing the radial profiles of C I in comets and fitting them with coma models, we measure the lifetime of atomic carbon against ionization processes in interplanetary space.

The majority of the C I measurements to date have been conducted by instruments on sounding rockets, *IUE* and *HST*, which have small fields of view (FOVs) relative to the typical angular extent of the C I emission. Exceptions to this have been objective grating spectra of comet C/1975 V1-A (West Smith et al. 1980), narrowband wide-field images of comet C/1995 O1 (Hale-Bopp) recorded by *Polar* spacecraft (Brittnacher et al. 2001), Wide Field Imaging Survey Polarimeter (*WISP*)

sounding rocket observations of comet Hale-Bopp (Harris et al. 1999), and imaging/spectro-imaging observations of Hale-Bopp by *MSX* (Kupperman 1999). With a technique similar to the one we use here, Kupperman found that the lifetime of atomic carbon was consistent with the solar photoionization lifetime of carbon calculated by Huebner et al. (1992). However, comet Hale-Bopp was a comet of unusual size. Several physical processes, including collisional heating in the dense inner coma (Combi et al. 1999; Harris et al. 2002) and gas phase chemical interactions between coma species (e.g., Glinski et al. 2004) acted to extend the distribution of coma species beyond what was expected using coma models based on comets with more typical production rates. Kupperman did not consider these effects. We use observations of comet C/2004 Q2 (Machholz), which is a much more “typical” comet. These observations suggest that the lifetime of carbon against ionization is about half of the photoionization lifetime calculated by Huebner et al. (1992). This implies that another process, which we show to be solar wind ionization, is comparable.

2. Observations

The Galaxy Evolution Explorer (*GALEX*) is a NASA Small Explorer (SMEX) mission designed to map the history of star formation in the universe (Martin et al. 2005; Morrissey et al. 2005, 2007). Its 1.2° FOV diameter and high sensitivity to extended sources also makes *GALEX* well suited to cometary coma studies. *GALEX* operates in two modes: direct imaging and objective grism imaging. Using a beam splitter and two detectors, *GALEX* images are simultaneously recorded in two bands: 1350–1750 Å (FUV) and 1750–3100 Å (NUV).

GALEX made both direct-mode and grism-mode observations of comet C/2004 Q2 (Machholz). The comet parameters are shown in Table 1. Over the course of the observations, the comet moved a substantial fraction of the *GALEX* 1.2° FOV, so we quote only the center of the spacecraft FOV, which was used for all observations. A log of observations is given in Table 2, which includes a background direct-mode image that was recorded a month earlier. Pipeline processing did not complete properly for grism orbit 3 due to a telemetry dropout, so we excluded it from our analyses.

The top two panels of Figure 1 show images created by the *GALEX* pipeline processing system. The 1657 Å multiplet is the dominant feature at all distances from the nucleus. Stars that appear as point sources in the direct-mode image are streaks in the grism-mode image since each stellar spectrum formed by the objective grism is individually imaged on the detector. On this scale, the comet motion is not readily apparent, but must be considered in order to provide high-quality radial profiles of the direct-mode image and co-add all of the grism images.

3. Data Reduction

The *GALEX* MAMA imagers detect and time tag individual photons. The photon lists are telemetered to the ground along with the spacecraft aspect information. Using reference stars in

Table 1. Observational Parameters

Parameter	Value
Comet observed	2005-03-01
Heliocentric distance	1.3 AU
Heliocentric velocity	11.0 km s ⁻¹
Heliographic lat.	30.3°
Heliographic lon.	141.0°
Geocentric distance	0.75 AU
FOV R.A.	4 hr 13'50,"
FOV Dec.	82° 45'10"

Table 2. Log of *GALEX* comet C/2004 Q2 (Machholz) observations used in this work

Type	Name ^a	Exp time (s)	Date	Start Time
Back. direct	1-fd-x.fits	271	2005-01-30	03:04:42
Comet direct	2-fd-x.fits	1635	2005-03-01	19:29:19
Comet grism	1-fg-x.fits	1618	2005-03-01	11:16:19
Comet grism	2-fg-x.fits	1619	2005-03-01	12:54:57
Comet grism	4-fg-x.fits	1619	2005-03-01	16:12:13
Comet grism	5-fg-x.fits	1619	2005-03-01	17:50:51

^afilename prefixes are G11_104001_COMET_2004Q2_000

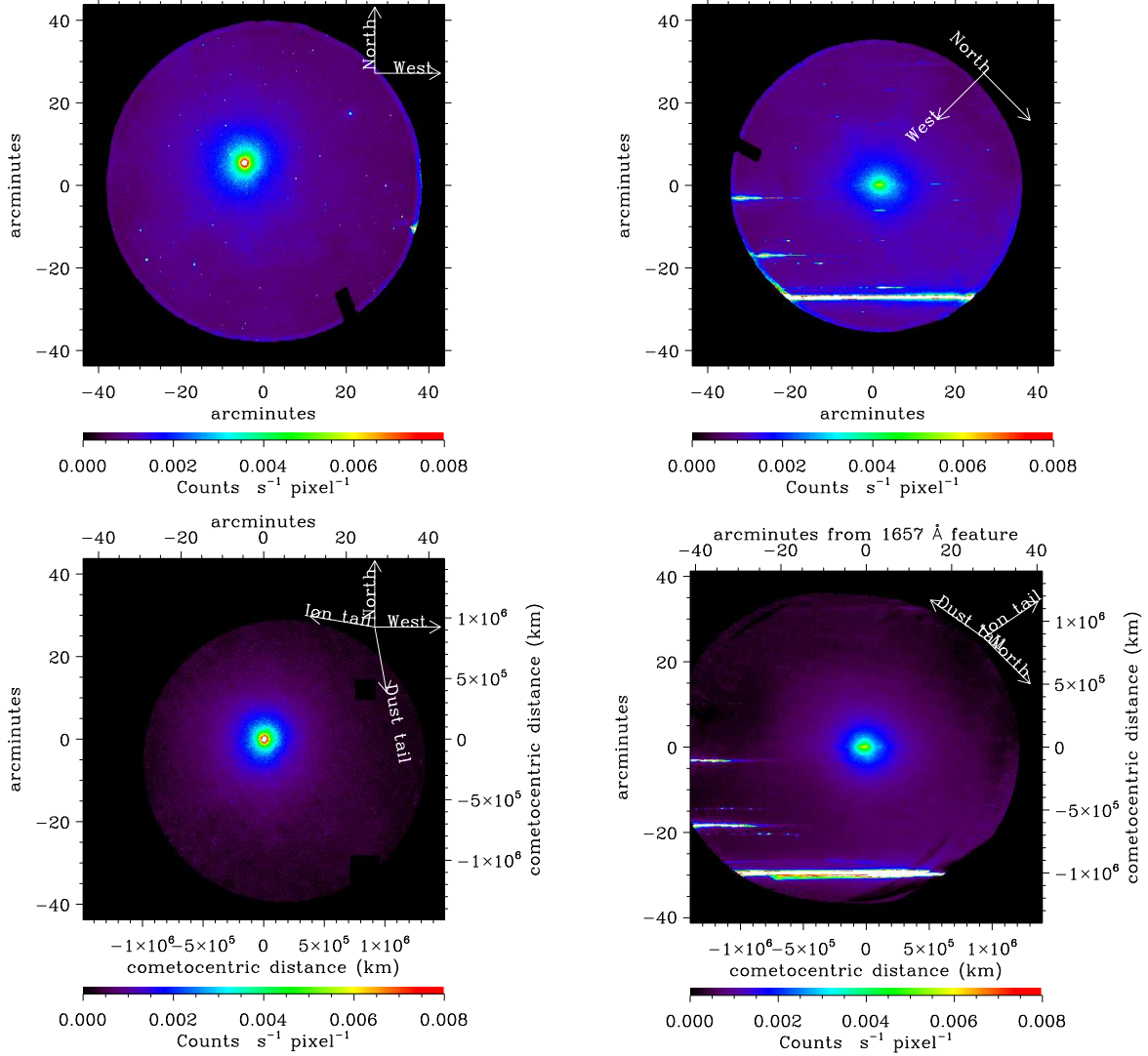


Fig. 1.— Top left: *GALEX* default pipeline processed direct-mode comet Machholz FUV image. Top right: the same, but grism-mode orbit 1. Bottom left (direct-mode) and right (grism-mode): images reconstructed in the frame of the comet, with background sources removed, and diffuse background subtracted, as described in §3. Four grism-mode observations are co-added (note trailing of FOV). The grism-mode images have been oriented so that the dispersion direction is horizontal and longer wavelengths are found to the right. Note that three bright stars off the edge of the FOV have been dispersed by the grism into the FOV.

the FOV, the astrometric solution is refined to better than $0.6''$ (Morrissey et al. 2007). In the reference frame of the stars, comets are trailed during the ~ 1500 s *GALEX* observing segments (“visits”). When several orbits are available, comets appear multiple times across co-added images. To eliminate comet trailing and multiple comet images, we used astrometrically corrected photon lists and an accurate comet ephemeris to cast photons into a comet frame of reference, which trails the stars. We obtain high-precision comet ephemerides from the JPL HORIZONS system using “@galex” as the observatory, which ensures that effects such as *GALEX* orbit parallax are properly considered. All coordinate transformations were done using the IDLASTRO routines.¹

Comet motion across the *GALEX* FOV and a mask that blocks out background sources allows us to completely remove flux from identified background sources. We used direct-mode observations of the same star field recorded a month before the Machholz arrived to create a high quality background source mask. Sources were identified by Emmanuel Bertin’s SExtractor package² that is run as part of the normal *GALEX* pipeline.

For the direct-mode observation, masks were created using the extreme corners of the sources tabulated in the SExtractor catalog columns XMIN, XMAX, YMIN, and YMAX. The mask was used to blank out the background sources in separate count and exposure time images that were accumulated as the photon lists were read. The mask was applied every time the predicted position of the comet moved 1 pixel relative to the background sources. The *GALEX* flat-field image was applied to the exposure image in a similar way. When the end of the photon list was reached, the count image was divided by the exposure image to produce a flat-fielded count rate image with the background sources effectively erased. The FOV of this image was extended in the direction of comet motion in the same way that the stars were trailed when we did not mask them.

For the grism-mode observations we converted the individual source masks into rectangles elongated in the dispersion direction and proceeded with the reduction in the same way as with the direct-mode for each visit individually. Photometrically correct addition of the four grism visits was achieved by adding count and exposure-time images and then dividing the results. Because the grism can disperse light from stars that are out of the FOV, our method of working from sources cataloged in the direct-mode image did not always produce masks for stars. These stars could easily be masked by hand or by modeling the comet emission (described in §4), subtracting it from the comet image cast in the reference frame of the stars by a procedure similar to which the stars are masked and inspecting the residuals for sharp features. For the purposes of this work, stars left in the image did not prove to be problematic.

In order to assure that our method of processing the *GALEX* photon list was consistent with that of the default *GALEX* pipeline, we ran our software without the comet ephemeris and without masking the stars. We found minimal count rate differences between our images and pipeline images,

¹<http://idlastro.gsfc.nasa.gov/>

²<http://sextractor.sourceforge.net/>

except within 100 $1.5''$ pixels of the edge of the circular FOV. We attribute this to details in the flatfielding process. In order to avoid detector burn in, the *GALEX* spacecraft executed a $1.5'$ spiral motion during pointed observations (Morrissey et al. 2005). The default *GALEX* pipeline applied the detector flat in the detector coordinate system every few seconds while images were being reconstructed in an astrometric coordinate system. The effect of the spiral motion on the flat-fielding at the edge of the FOV was therefore correctly considered. The flat-field provided to guest observers by the *GALEX* project is an average of the detector flat over each orbit. Our method of applying this flat therefore did not take into consideration the spiral motion. The flat changes slowly as a function of position except at the edges, so the differences in flat-fielding methods does not effect the quality of the data except at the edges. As the *GALEX* images are 3840×3840 pixels, we simply masked out the 100 pixel wide annulus when we were applying the flat-field corrections in our procedure.

The lower-left panel of Figure 1 shows the resulting direct-mode image with the background discussed in the next section subtracted. The removal of discrete sources has been highly successful. The lower-right panel of Figure 1 shows the corresponding grism-mode image, which is a co-add of 4 visits.

3.1. Background

Since the comet emission filled the field-of-view, it was not possible to estimate the contribution of the background from the comet image itself. We used the background image recorded a month before the comet image for this purpose. Discrete sources were removed using the mask generated from the SExtractor catalog. In order to fill in the missing data where the sources were removed, we smoothed the image using a 100×100 pixel boxcar average. The resulting image was translated to the average R.A. and DEC of the comet during the direct-mode observation.

Before subtracting the image from the data, we checked for any effects that might contribute to variation of the background level over the course of one month. Sujatha et al. (2009), in studying multiple *GALEX* observations of the Sandage nebulosity show that in the FUV, airglow from the 1356 \AA and possibly 1304 \AA lines is responsible for the primary variation in the total *GALEX* count rate as a function of time over short and long timescales. Figure 2 shows the count rate in the *GALEX* FUV detector for the comet (upper curve) and background (lower curve) after removal of detector effects such as hot spots. The sinusoidal variation is induced by the combination of a bright star near the edge of the FOV and the spiral motion of the *GALEX* spacecraft. Otherwise, the count rate curves resemble the parabolæ described by Sujatha et al. (2009). We adapted the their method to estimate the *difference* between the airglow contribution in the comet image and the background image: $-5.66 \times 10^{-5} \text{ counts s}^{-1} \text{ pixel}^{-1}$. The primary contribution to the difference in the airglow contribution came from the fact that the background image was recorded only on the steep part of the count rate curve, so its average airglow was high compared to the comet observation, which covers the entire parabola.

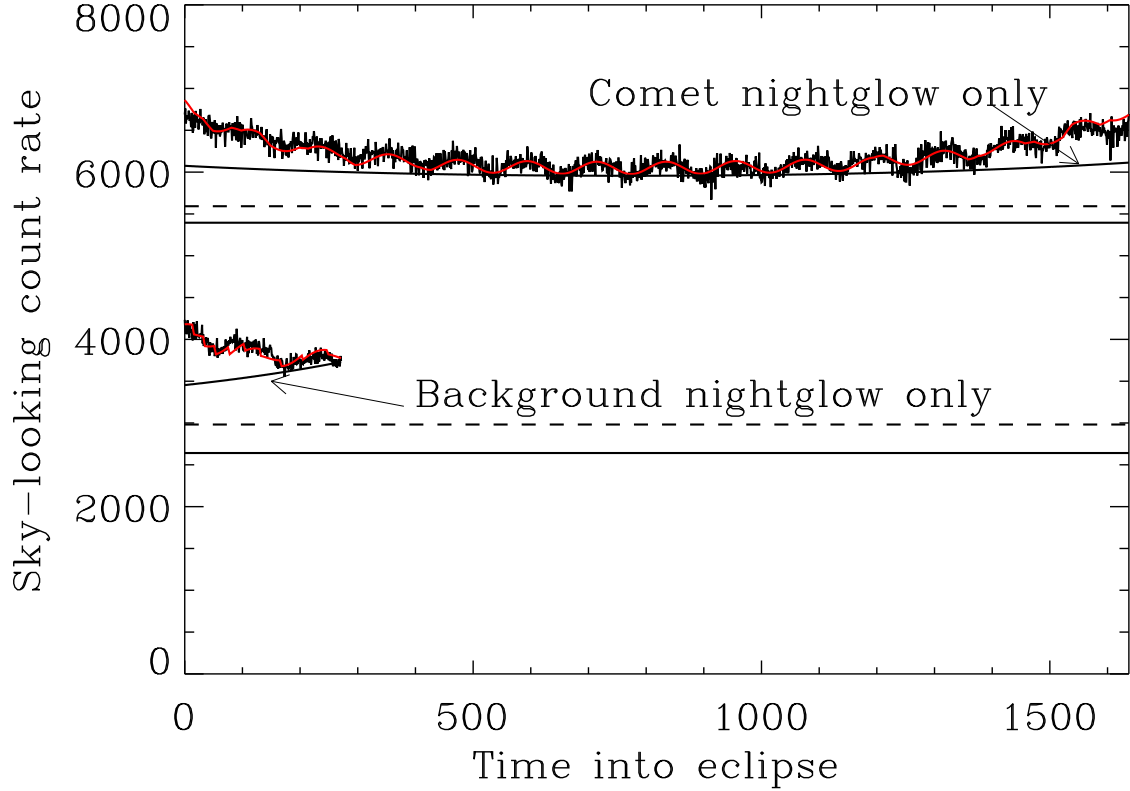


Fig. 2.— Count rate in the *GALEX* FUV detector for the comet (upper data points) and background (lower data points) visits. The count rate has been corrected for detector effects such as hot spots. The sinusoidal variation in the signals is due to a bright star near the edge of the FOV and the spiral motion of the *GALEX* spacecraft. The model described in the text plus the sinusoid is overplotted in red in both cases. The model with $B = 1$ (nightglow only) is overplotted to demonstrate the relative contributions of the day and nightglow signals. The average astrophysical signal without airglow is plotted as the straight lines for the two cases described in the text: $\rho_0 = 0.7$ (solid) and $\rho_0 = 0.5$ (dashed).

We note that the Sujatha et al. (2009) method is largely empirical and must be repeated for each observing geometry. The comet and the Sandage nebulosity were both high-dec sources, so we expect our use of their parabolæ to be reasonably accurate. However, the sensitivity of our lifetime measurement to the precise value used for the background motivated us to investigate the airglow effect more carefully. We demonstrate here that a simple atmospheric model, geometric considerations of earth shadow on the atmosphere and accurate consideration of observing geometry, explains the variation in *GALEX* count rate seen during each eclipse period. Much like photometric data taken at various zenith distances, our method can be used to independently remove the effects of airglow from *any GALEX* eclipse.

We constructed a model atmosphere using an exponential rooted in the F-region (altitude 300 km) with an initial density ρ_0 (detected *GALEX* FUV counts per km at an altitude of 300 km) and a scale height, h . We assumed that the distribution was the same over every point on the Earth but we defined a unitless “day boost” parameter, B , which multiplied the density of emitters when they were in sunlight. We used the orbit of *GALEX* described by two line elements (TLEs) archived at <http://www.spacetrack.org> to determine the position of the satellite as a function of time, a solar ephemeris provided by the SUN-POS.PRO module of the IDLASTRO routines, and a simple stepwise integrator to compute the airglow brightness for each line of sight as a function of time into the visit. The final component of the model was the astrophysical count rate, which we assumed to be constant over the visit. The red solid lines in Figure 2 show the resulting best-fit model, including the sinusoid discussed above. Our model gave good fits for a range of parameters corresponding to airglow *differences* of -5.57×10^{-5} counts s⁻¹ pix⁻¹ to -3.6×10^{-5} counts s⁻¹ pix⁻¹. An interesting extension to this exercise would be to use more sophisticated ionospheric and plasmaspheric models to derive the airglow emitter profiles and increase the accuracy of the *absolute* airglow determination.

Having derived a best-fit background image, we subtracted it from the comet image. There was a slight oversubtraction around the edges due to the background image smoothing and the elongation of the comet image. The effected points were removed with an annular mask 175 pixels wide. Residual emission around the hot spot in the southwest portion of the image and a bright source toward the west were also masked. The resulting image is shown in the lower-left panel of Figure 1. The co-added grism-mode images formed by our reduction procedure are shown in the lower-right panel of Figure 1 with diffuse background determined in §4 subtracted.

4. Analysis

We used the combination of *GALEX* direct and grism-mode data to measure the carbon ionization lifetime. We began by assuming that C I emission dominates the passband at all cometocentric distances and that CO is the sole parent molecule. As discussed by Huebner et al. (1992) and Tozzi et al. (1998), CO dissociates in significant amounts into both ground state carbon, C(³P) and the metastable state C(¹D). C(¹D) decays to C(³P) in 4077 s (a rate of 2.45×10^{-4} s⁻¹), inde-

pendent of heliocentric distance (Hibbert et al. 1993). $C(^1D)$ can be photoionized with a predicted rate that is ~ 10 times faster than that of $C(^3P)$ (Huebner et al. 1992). However, the resulting photoionization lifetime, 2.8×10^5 s (rate of $3.6 \times 10^{-6} \text{ s}^{-1}$), is still long (rate is slow) compared to the metastable lifetime (rate), so for the purposes of this work, we neglect the time spent in the metastable state and assume all of the CO dissociates directly to $C(^3P)$. In §4.1, we explore the differences in the photochemical ejection velocities of $C(^3P)$ and $C(^1D)$, which could, in principle, affect our results, and find them to be small ($\sim 25\%$).

We fit two-component Haser models to radial profiles formed from our background-subtracted direct-mode image (4.1, Fig. 3). We did this as a function of airglow offset in order to estimate the effect of our background subtraction uncertainty on the carbon lifetime (Fig. 4). We find that the lifetime measured by this method agrees well with the theoretical carbon ionization lifetime calculated using values for solar wind and photoionization tabulated by Rubin et al. (2009) assuming comet Machholz was in the slow solar wind (Fig. 4, Table 3).

Figure 3 shows radial profiles of four quadrants of the background-subtracted direct-mode comet image shown in the lower-left panel of Fig. 1. Quadrant 4 is centered on the dust tail, quadrant 1 is oriented 90° counter-clockwise from quadrant 4, etc. The profiles were created using an adaptive binning ring-sum algorithm similar to that described by Harris et al. (2002). For the profiles shown in Figure 3, at least 1000 counts per radial bin were used. For our fitting exercises, there were at least 10,000 counts per bin. The profiles show good agreement except for the one oriented toward the dust tail.

4.1. The Haser model

Haser (1957) first solved the simple differential equation which describes the radial distribution of a species traveling radially away from a comet nucleus at velocity v_{bulk} and with lifetime against destruction, τ_p . A similar differential equation can be solved for the case of a daughter species, resulting in the 2-component Haser model (e.g., Krishna-Swamy & Brandt 1986). A critical component of the 2-component Haser model is the ejection velocity, v_e , of the daughter from the parent molecule. Festou (1981) pointed out that the common usage of v_e in the Haser model was unphysical: the daughters were frequently assumed to be ejected radially outward from their parents, when in fact, they would be emitted isotropically from the point of destruction of the parent. The vectorial model of Festou (1981) addresses this shortcoming. Many workers have noted that the 2-component Haser model provides good fits to comet profiles of daughter species. The problem is mapping the input parameters of the Haser model (e.g., parent and daughter outflow velocities) to independently determined quantities (e.g., parent outflow velocity and daughter ejection velocity). Combi et al. (2004) provide formulæ for this mapping that allow the computationally simple Haser model to be used to emulate the more sophisticated models. We use the Combi et al. (2004) formulæ in all our calculations.

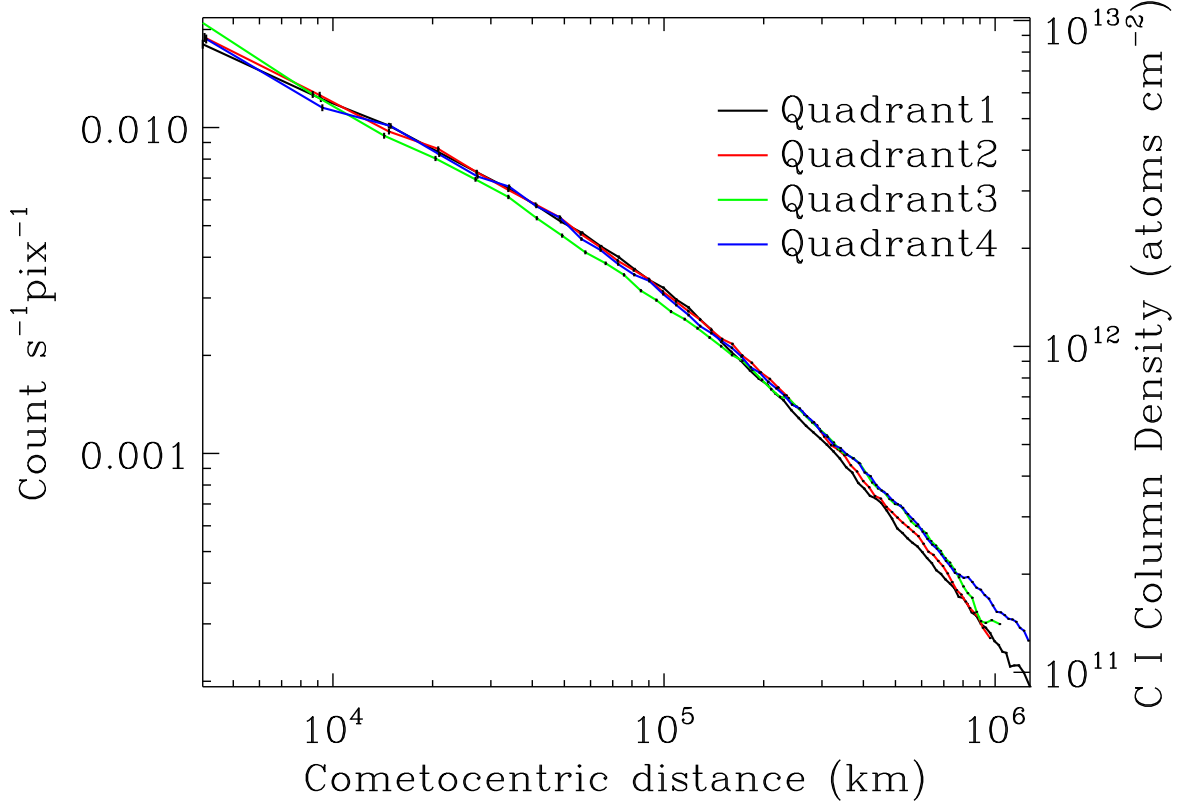


Fig. 3.— Quadrant-by-quadrant radial profiles of comet Machholz FUV emission. The left-hand Y-axis shows the background-subtracted average count rate per pixel in each radial bin. The right-hand Y-axis shows the count rate converted into C I column density using the g -factors described in the text and the assumption that all of the emission in the FUV band is from C I. Quadrant 4 is centered on the antisunward or “Dust tail” direction, as indicated in the lower-left panel of Fig. 1. Quadrant 1 is counterclockwise from quadrant 4, etc. Statistical error bars (total vertical extent $2\text{-}\sigma$) are shown and are comparable to the line widths.

As outlined above, our starting point was to assume CO is the sole parent of C I. We also assume CO is produced within the collision sphere and thermalized to the bulk outflow velocity, v_{bulk} , of the coma. Preliminary analysis of our contemporaneously recorded *GALEX* NUV data suggests that comet Machholz had a water production rate in the $\log(Q(\text{H}_2\text{O})) = 28 - 29$ range. According to the formulæ given by Budzien et al. (1994) and Tseng et al. (2007), this translates into $v_{\text{bulk}} = 0.74 \text{ km s}^{-1}$ and 1.02 km s^{-1} , respectively at the comet’s heliocentric position. Combining the Huebner et al. (1992) CO photodissociation rate and Rubin et al. (2009) CO solar wind ionization rates results in a total solar quiet CO lifetime of $7.9 \times 10^5 \text{ s}$ (rate of $1.3 \times 10^{-6} \text{ s}^{-1}$). Tozzi et al. (1998) use an improved set of calculations and find a solar maximum CO photodissociation lifetime of $4 \times 10^5 \text{ s}$ ($2.5 \times 10^{-6} \text{ s}^{-1}$). We estimate the solar minimum CO lifetime to be $\lesssim 5 \times 10^5 \text{ s}$ ($\gtrsim 2 \times 10^{-6} \text{ s}^{-1}$).

As discussed above, we can neglect ionization out of the $\text{C}^{\text{(1D)}}$ state because the metastable lifetime is so much shorter than the ionization lifetime, however, we must check to see if the ejection velocities, v_e , of $\text{C}^{\text{(3P)}}$ and $\text{C}^{\text{(1D)}}$ from CO are sufficiently different to require individual consideration. Huebner et al. calculate $v_e = 4.9 \text{ km s}^{-1}$ and 3.9 km s^{-1} , respectively. Tozzi et al. find the ejection velocity, v_e , of $\text{C}^{\text{(3P)}}$ from CO to be 4 km s^{-1} . Tozzi et al. do not directly calculate v_e values for $\text{C}^{\text{(1D)}}$, but rather adopt a range of values from v_{bulk} to 3.9 km s^{-1} . We used a less conservative lower limit and assumed that the $\text{C}^{\text{(1D)}}$ v_e value is within 25% of the $\text{C}^{\text{(3P)}}$ v_e value, as suggested by the Huebner et al. calculations. As discussed below and shown in Figure 4, this is comparable to the uncertainty in our fitting and background removal activities, so we neglect it.

The formula of Whipple & Huebner (1976) shows that the collision sphere, over which gas interactions transfer excess energy between gas species, was $\sim 2500 \text{ km}$ for Machholz. This is much smaller than scale lengths of CO or any of the major carbon parent molecules. Thus, the motion of carbon is dominated by its ejection velocity. Since v_e is significantly larger than v_{bulk} , the Combi et al. (2004) formulæ show that the daughter lifetime that would be derived from sophisticated models is essentially unaltered from that which is derived from the Haser model. Conversion of our measured Haser scale lengths to the C I lifetime is a simple matter of dividing by the assumed ejection velocity.

We used MPFIT (Moré 1978; Markwardt 2009) to fit two-component Haser models to the profiles. Because the statistical errors on the profiles we were fitting were so small, the formal errors of all the parameters were always less than 1%. The off-diagonal elements of the correlation matrix were also always less than 1%. The two-component Haser model was able to accurately reproduce all of the profiles in Figure 3 except for the inner-most point, which consistently fell above the model.

We experimented with excluding data below small cometocentric distances, r_{min} to see if this effected the C I lifetime. As r_{min} was increased from 0 to $1 \times 10^5 \text{ km}$, there was a 20% decrease in the measured C I lifetime. Finding this to be an acceptable range of uncertainty in the fitting exercise, we choose the midpoint, $5 \times 10^4 \text{ km}$ as our best value and proceeded with the other experiments

described below.

Next, we varied r_{\max} , the upper cutoff of the data we fit, and the assumed airglow offset value. We created contour plots of the C I lifetime in the plane of airglow offset versus r_{\max} for a variety of combinations of quadrants. We found that quadrant 1 resulted in the most consistent behavior as a function of r_{\max} . For all $r_{\max} > 3 \times 10^5$ km, in quadrant 1 all the measured C I lifetime values fell within 10% of each other. This is important. It means that the *GALEX* FOV, which extends to $\sim 1.1 \times 10^6$ km is large enough to reliably measure the carbon scale length, even though at this heliocentric distance, it was larger than the *GALEX* FOV.

Figure 4 summarizes our fitting exercises. The C I lifetime is plotted against the assumed offset between the comet and background airglow levels. The plot was made by fitting quadrant 1 data between $r_{\min} = 5 \times 10^4$ km and $r_{\max} = 1.1 \times 10^6$ km (the largest radial bin containing at least 10,000 counts). It is at the edge of the radial distribution that the background subtraction accuracy becomes particularly important, as any over/undersubtraction is directly reflected as a change in the number density of CI and therefore the scale length. We mark the two values of the airglow offset level discussed in §3.1 with the solid and dashed lines. The resulting 1 AU C I lifetimes are 7.1 and 9.6×10^5 s for the “best” and minimum cases, respectively. These correspond to total ionization rates of 1.4 and $1.0 \times 10^{-6} \text{ s}^{-1}$, respectively. Table 3 summarizes these results.

4.2. Comparison to physical processes

Photoionization is generally assumed to be the dominant ionization process for most cometary molecules and radicals, however, for long-lived species such as carbon and oxygen, solar wind ionization processes become non-negligible (e.g., Axford 1972; Rubin et al. 2009). We find that for carbon, solar wind ionization processes are comparable to photoionization. Table 3 summarizes calculations of carbon ionization lifetimes (rates) from the dominant physical processes for a variety of solar conditions. We observed comet Machholz near the end of solar cycle 23, so we assume quiet sun conditions from the perspective of the photon field. The heliographic latitude of Machholz was 30° , so Machholz was likely on the upper edge of the slow solar wind zone identified by *Ulysses* and *SOHO* SWAN observations (Smith & Marsden 1995; Bzowski et al. 2003). Our measured ionization lifetime of $7.1 - 9.6 \times 10^5$ s ($1.0 - 1.4 \times 10^{-6} \text{ s}^{-1}$) therefore compares favorably with the predicted lifetime of 8.2×10^5 s ($1.2 \times 10^{-6} \text{ s}^{-1}$). In Figure 4, we present a graphical interpretation of these results combined with the presentation of our most easily identified systematic uncertainty: determination of the relative contributions of airglow in the comet and background images.

4.3. Grism Image analysis

In §4.1 we described Haser model fits to the direct-mode profiles and showed that the measured C I lifetime was relatively stable as a function of r_{\min} and r_{\max} (20%). However, these fits all

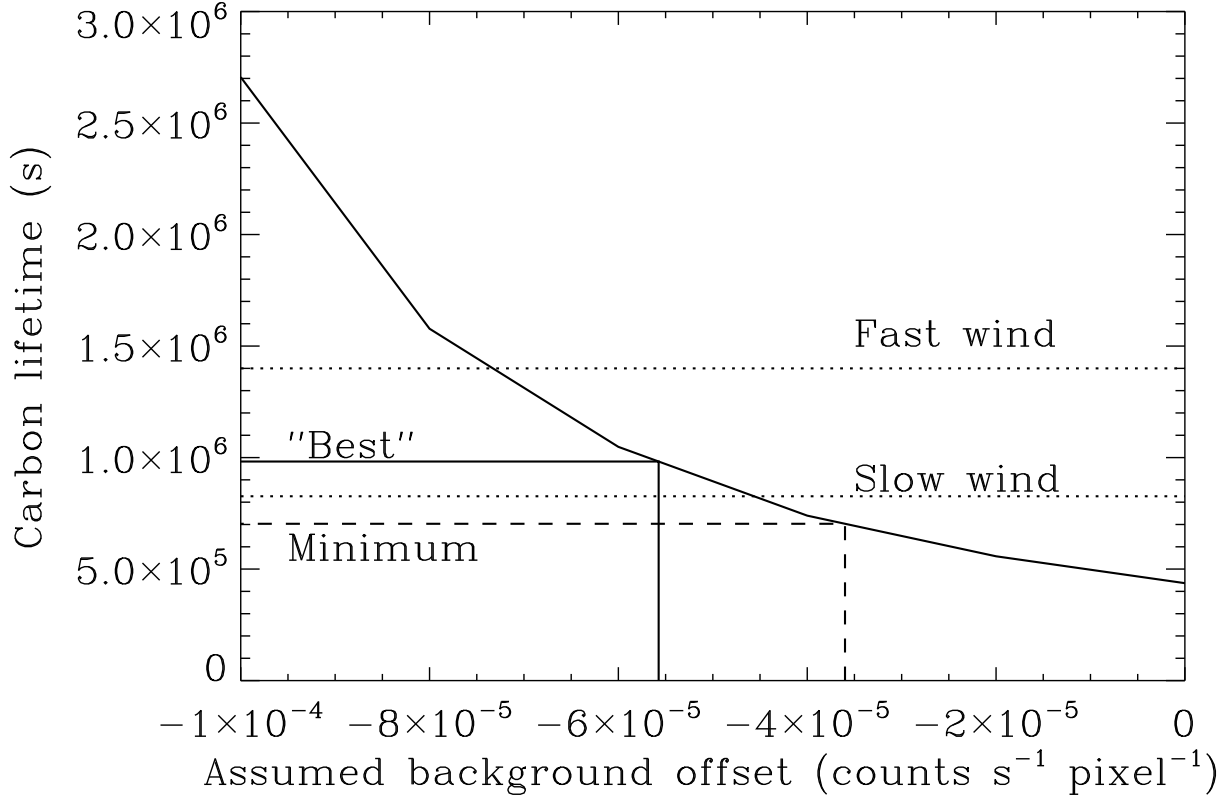


Fig. 4.— Carbon lifetime at 1 AU vs. assumed background offset between the comet and background direct-mode images. The best-estimate value of our background offset calculated in §3.1 to be -5.57×10^{-5} counts s^{-1} pixel $^{-1}$ is shown as the solid vertical line. The resulting carbon lifetime is similarly indicated graphically and labeled “Best.” The minimum background offset is indicated in this way with the dashed lines. The calculated values of the carbon lifetime from the first two columns of Table 3 are shown as dotted lines. The data indicate that during our observations, comet Machholz was embedded in the slow solar wind.

required a parent scale length that was extremely short, indicating the presence of contamination from the shorter-lived species in the *GALEX* FUV bandpass. We use a preliminary analysis of the *GALEX* grism-mode data to identify the species contributing the contaminating emission and demonstrate that this contamination is unlikely to effect our C I lifetime measurement.

The general method we use for analyzing the grism-mode images is forward modeling. We create a radial profile of the expected emission in a particular line or spectroscopically unresolved band. Our software is structured so that any model profile can be used, but for these analysis, we use the 1 or 2-component Haser model, as appropriate, with scale lengths modified by the formulæ of Combi et al. (2004) to emulate the output of more sophisticated coma models. The profile is scaled by the product of the production rate, the g -factor of the feature in question (see below and Table 4) and the effective area of the *GALEX* instrument at the wavelength of the feature (Morrissey et al. 2007)³. We then create a figure of rotation from the profile, thus transforming the profile into a coma image. We offset the image according to the *GALEX* grism dispersion relation from the astrometric center of the comet, determined by our reduction procedure described in §3. Next, we convolved the image by an estimate of the *GALEX* point spread function in grism-mode, which we create by making a figure of rotation from the cross-dispersion profile model generated from stellar spectra in the grism-mode image by the *GALEX* pipeline processing system. We then repeated the process of converting the model profile into a coma image for each of the three primary *GALEX* grism orders and summed the results.

We calculated g -factors at 1 AU and a heliocentric velocity of 11 km s^{-1} using a high-resolution solar spectrum from the Solar Maximum Mission normalized to absolute fluxes measured by *SOLSTICE* together with absorption oscillator strengths available from NIST. For the purposes of these calculations, we assumed optically thin conditions. The implications of this assumption, particularly for CO, are discussed below. The CO g -factors were calculated assuming an excitation temperature of 70 K. The g -factors and *GALEX* grism mode effective areas are listed in Table 4.

We determined the background level in our grism-mode data by subtracting a preliminary model of the C I emission based on the direct-mode analysis. We assumed that CO was the sole parent of C I and used the same C I production rate, $Q(\text{C}) = 2.8 \times 10^{28} \text{ s}^{-1}$, found in our direct-mode analysis. After experimenting with $Q(\text{C})$, and the C I scale length, we found that the grism-mode background was much higher than expected assuming the value from the direct-mode image and the ratio between the total efficiencies of the two modes. We attribute the high background to emission from the unmasked sources discussed in §3. We found a best-fit background level of $5.4 \times 10^{-4} \text{ counts s}^{-1} \text{ pixel}^{-1}$. The top two panels of Figure 5 shows the inner $2 \times 10^5 \text{ km}$ of our *GALEX* grism-mode data before (left) and after (right) the C I subtraction. The positions of the major features in the primary *GALEX* FUV grism order have been indicated.

After subtraction of the C I emission, a pseudo-continuum was evident (upper right-panel of

³<http://galexgi.gsfc.nasa.gov/docs/galex/Documents/PostLaunchResponseCurveData.html>

Table 3. Carbon Ionization Lifetimes (Rates) at 1 AU

Process	Ionization Lifetime $\times 10^5$ s (Rate $\times 10^{-6}$ s $^{-1}$)			Reference
	Quiet Sun	Quiet Sun	Active Sun	
	Slow Wind ^a	Fast Wind ^b	Slow Wind ^a	
$C + h\nu \rightarrow C^+ + e^-$	24 (0.41)	24 (0.41)	10 (0.92)	Huebner et al. (1992)
$C + H^+ \rightarrow C^+ + H$	17 (0.59)	40 (0.25)	17 (0.59)	Rubin et al. (2009)
$C + e^- \rightarrow C^+ + 2e^-$	48 (0.21)	20 (0.05)	48 (0.21)	Rubin et al. (2009)
Total predicted	8.2 (1.21)	14 (0.71)	5.8 (1.72)	
Measured	7.1 – 9.6 (1.0 – 1.4)			

^a $v = 400$ km s $^{-1}$, $n_e = 10$ cm $^{-3}$

^b $v = 750$ km s $^{-1}$, $n_e = 2.5$ cm $^{-3}$

Table 4. g -factors at 1 AU

Feature	g -factor ^a	Eff. Area ^b
C I 1561 Å	0.93	18.9
C I 1657 Å	4.22	11.5
CO total	0.16	14.9
S I 1425 Å	0.29	8.9
S I 1475 Å	0.25	21.6
S I 1813 Å	4.90	2.5

^a $\times 10^{-5}$ phot s $^{-1}$ particle $^{-1}$

^bGrism-mode peak order, cm 2

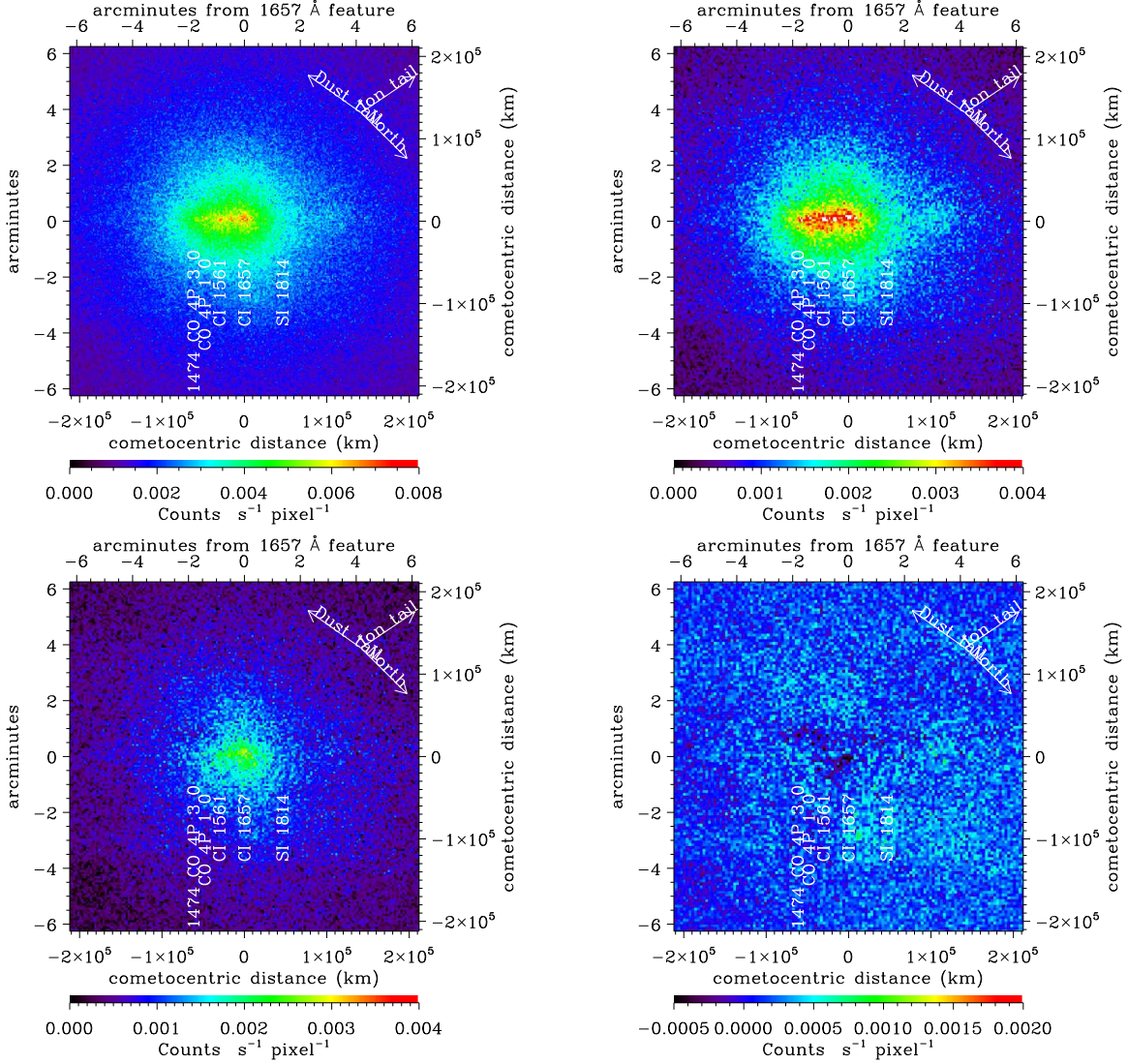


Fig. 5.— Machholz FUV grism-mode analysis. The frames show the inner 2×10^5 km of the co-added comet Machholz *GALEX* grism-mode images in various stages of residual subtraction. Background described in the text has been subtracted from all frames. The primary grism order positions of the brightest features in the FUV bandpass have been marked. Top left: no model subtraction. Top right: subtract C I from a CO parent with $Q(C) = 2.8 \times 10^{28} \text{ s}^{-1}$. Bottom left: also subtract CO, with the profile described in the text and $Q(\text{CO}) = 3.0 \times 10^{28} \text{ s}^{-1}$. Bottom right: modify original $Q(C)$ to $1.8 \times 10^{28} \text{ s}^{-1}$, $Q(\text{CO}) = 2.8 \times 10^{28} \text{ s}^{-1}$ and subtract $Q(C) = 1.2 \times 10^{28} \text{ s}^{-1}$ from CH_4 . To increase the signal to noise ratio in the residual images, they have been binned by 3×3 , 3×3 , and 4×4 pixels, respectively. Also note changes in color bar limits.

Fig. 5). Since dust emission near the nucleus is negligible in the FUV, we took this to be emission from the more than 80 lines of the CO Fourth Positive system that fall in the *GALEX* FUV band-pass. Most of these lines have been resolved and well studied by previous high resolution long-slit spectroscopic observations (e.g., McPhate et al. 1999; Lupu et al. 2007). Lupu et al. model the CO Fourth Positive emission as a function of cometocentric distance to 3,000 km with and without considering self-absorption (optical depth) effects. They find evidence for detectable optical depth effects in the inner ~ 1000 km of comets with production rates similar to that of Machholz. Perhaps not surprisingly, when we subtracted a one-component Haser model of the CO emission from our C I residual, there was obvious over-subtraction at cometocentric distances $< 10,000$ km. We emulated optical depth effects by using a 2-component Haser model with an effective parent lifetime of 10,000 s (rate of $1 \times 10^{-4} \text{ s}^{-1}$) at 1 AU. The resulting residual, assuming $Q(\text{CO}) = 3.0 \times 10^{28} \text{ s}^{-1}$ is shown in the lower-left panel of Figure 5. Since we assumed optically thin conditions, our fit is not sensitive to whether or not CO comes from a nucleus-native source or is formed from a distributed source (e.g., Eberhardt et al. 1987; Di Santi et al. 2001; Brooke et al. 2003; Lupu et al. 2007; Bockelée-Morvan et al. 2010). We look forward to further work on this subject as we incorporate radiative transfer calculations in our CO profile calculations and improve our grism background source cleaning technique.

After subtracting the primary C I and CO sources, residual emission, centered roughly on C I 1657 Å was evident. This was not an artifact of the unexpectedly large grism background discussed above. It is reasonably well described by C I from a parent with an effective 1 AU lifetime of 1×10^5 s (rate of $1 \times 10^{-5} \text{ s}^{-1}$), assuming CO has a lifetime of 5×10^5 s ($2 \times 10^{-6} \text{ s}^{-1}$; see §4.1). We experimented with various CO lifetimes ranging from 2×10^5 s (which happened to describe a large section of our data well) to 7.9×10^5 s (Rubin et al. 2009). These CO photodissociation lifetimes correspond to rates of 5 and $1.3 \times 10^{-6} \text{ s}^{-1}$, respectively. The problem with a very short CO lifetime is that if all of the C I came from CO, the model clearly over-subtracted inside of 2×10^4 km. From this we deduced that the dominant carbon parent molecule cannot have a lifetime as short as 2×10^5 s ($5 \times 10^{-6} \text{ s}^{-1}$) and that at least one more carbon parent molecule was needed.

Knowing that we needed at least one other carbon parent molecule besides CO to provide C I emission inside 2×10^5 km, we turned to infrared observations of comet Machholz to provide suggestions. Based on the work of Bonev et al. (2009) and Kobayashi & Kawakita (2009), CH_4 and CH_3OH were the most likely candidates. Our estimates of the maximum production rates of atomic carbon from CO and these molecules is shown in Table 5. Of particular note is our adoption of the Huebner et al. (1992) CO branching ratios even though we use the Tozzi et al. (1998) CO lifetime. According to Huebner et al., a significant amount of CO is lost to ionization, leaving only 50% for C I emission. Tozzi et al. find a significantly shorter total CO lifetime than Huebner et al. but do not calculate rates into the various branches.

The detailed photodissociative lifetimes and excess energies of the CH_4 to carbon chain are not known. Huebner et al. (1992) calculate the photo rates of the various channels of CH_4 to its daughters and the excess energies of these reactions. The total solar quiet lifetime of CH_4 is

Table 5. Carbon Parent Molecule Candidates

Parent Molecule	% CO	$Q(C)_{\max}$ ($\times 10^{28} \text{ s}^{-1}$)	$Q(C)$ ($\times 10^{28} \text{ s}^{-1}$)	τ_p ($\times 10^5 \text{ s}$)	v_e (km s^{-1})
CO ^a	100	...	2.8 ^a
CO	50 ^b	1.4	1.8	$\lesssim 5^c$	4 ^c
CH ₄	35 ^d	1.0	1.2 ^e	1.4	>3.1
CH ₃ OH	50 ^d	1.4	...	>5.9	4.5
C ^f	2.8 ^f	8 ^g	...

^aCO Fourth Positive emission

^bHuebner et al. (1992)

^cSee §4.1

^dBonev et al. (2009) and Kobayashi & Kawakita (2009)

^eDecreases to $1.0 \times 10^{28} \text{ s}^{-1}$ assuming CO lifetime of $3 \times 10^5 \text{ s}$

^fFrom direct-mode profile fit

^gCarbon lifetime from this work

1.3×10^5 s (7.7×10^{-6} s $^{-1}$). The primary channel to atomic carbon is through CH₂. The interstellar and solar photo rates of CH₂ have been calculated by van Dishoeck et al. (1996), who find the total lifetime is $7 - 11 \times 10^3$ s ($9 - 14 \times 10^{-5}$ s $^{-1}$). The majority of the CH₂ decays to CH, which, according to Huebner et al. (1992) has a very short lifetime (108 s; rate of 9.3×10^{-3} s $^{-1}$). Formally, a 4-generation Haser model would best describe the C I emission from CH₄. However, the progression of long to short parent-daughter lifetimes allows us to emulate the distribution with a standard 2-component Haser model, with the effective parent lifetime equal to the sum of all of the lifetimes (see Table 5). We mount a similar argument to estimate limits on the effective ejection velocity of carbon from the chain of CH₄ decay. From Huebner et al., the first and last links are 3 and 0.7 km s $^{-1}$, respectively, which add in quadrature to find 3.1 km s $^{-1}$. Excess energies of the CH₂ dissociations are not quoted by van Dishoeck et al. (1996), so 3.1 km s $^{-1}$ is a lower limit to the carbon ejection velocity from the CH₄ chain. When we created the model described below, we used 3.7 km s $^{-1}$, which assumes a 2 km s $^{-1}$ ejection velocity of CH from CH₂.

The CH₃OH lifetime is 8.7×10^4 s (1.1×10^{-5} s $^{-1}$) and dissociates primarily to H₂CO, which lives 4600 s (Huebner et al. 1992). H₂CO primarily dissociates to CO, so CH₃OH cannot provide the short-lived component of the C I emission. The ejection velocities of the daughters from the CH₃OH and H₂CO dissociations are 1.7 and 1 km s $^{-1}$, respectively, so, adding in quadrature with the carbon ejection velocity from CO, we find a total $v_e = 4.5$ km s $^{-1}$.

The fact that the final carbon ejection velocities we calculate for our three candidate C I parent molecules all lie within 25% of each other is significant. This means that after the details of the parent molecule dissociation are sorted out, the carbon from all of these sources will be traveling at roughly the same speed away from the nucleus of the comet. At large cometocentric distances, Haser models of these individual components will therefore be parallel to each other. This perhaps explains why the radial profiles shown in Figure 3 and Figure 6 follow the characteristic Haser profile outside of $\sim 3 \times 10^5$ km despite the fact that multiple sources of C I are present.

As a final test of our analyses, we constructed a three-component model consisting of CO Fourth Positive and two C I sources, one from CO and one from CH₄. The lifetimes and ejection velocities are discussed above and the best-fit production rates are shown in Table 5. The grism-mode residual is shown in the lower right-hand panel of Figure 5. The model, with its constituent parts is shown compared to the direct-mode quadrant 1 profile in Figure 6.

A final adjustment to achieve the best residuals to the grism-mode data was made by shifting the comet image 2 pixels in the positive dispersion direction. This corresponds to 3'', which is smaller than the 4.5'' GALEX FUV point-spread function and reasonable given the difficulty in finding high-precision astrometric solutions in the dispersion direction from stellar spectra at a spectroscopic resolving power ($\lambda/\Delta\lambda$) of 200.

Having achieved a good residual grism-mode image, we established an upper limit of $Q(S) = 2 \times 10^{26}$ s $^{-1}$, assuming the dominant parent of S is H₂S (e.g., McPhate et al. 1999) with lifetimes from Meier & A'Hearn (1997).

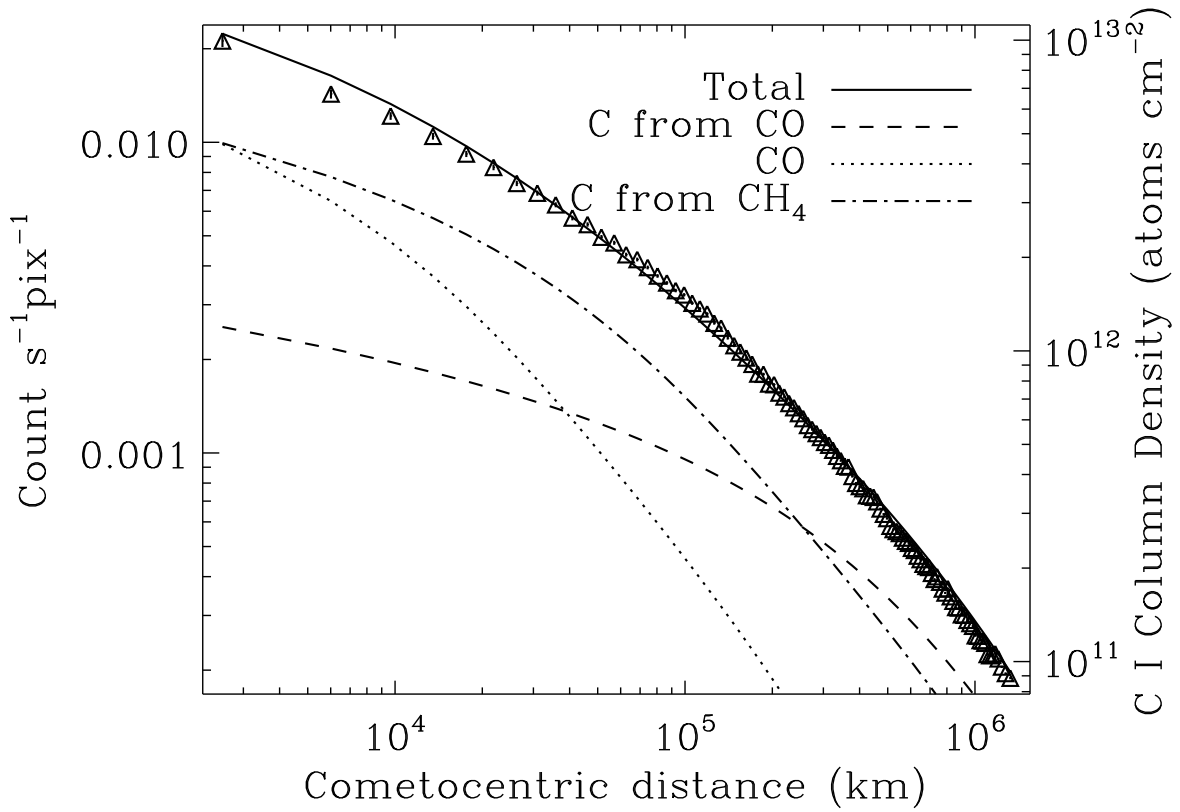


Fig. 6.— Radial profile from quadrant 1 using 500 counts per bin compared to the three-component model discussed in the text. Residuals of this model from the grism-mode data are shown in the lower right-hand panel of Figure 5.

5. Discussion

We have created a model of CO and C I emission that describes the *GALEX* direct and grism-mode observations of comet Machholz (Figs. 5–6). The model shows the surprising result that carbon from CH₄ dominates carbon emission from CO out to $\sim 2 \times 10^5$ km. At even greater cometocentric distances C I emission from CH₃OH may be significant. Since the carbon ejection velocities from all of these parent molecules is likely to be comparable (Table 5), the net effect of multiple carbon parent molecules on our carbon ionization lifetime measurement is negligible, as long as the *GALEX* FOV samples the region of the coma beyond the effective combined parent scale length (indicated by the “knee” in the two-component Haser model). Inspection of Figure 6 suggests that such a knee has been reached in the data at $\sim 2 \times 10^5$ km.

Carbon emission from CH₃OH, which dissociates to carbon through CO, will everywhere have a flatter distribution than carbon emission from CO and CH₄. If this emission is significant, the flat part of the parent distribution may flatten the total C I distribution. If this were the case, the carbon ionization lifetime measured by our method would be artificially long by some unknown amount. However, we estimate the total C I emission from CH₃OH will be no more than that of C I from CO (Table 5), so its contribution will be smaller inside some critical radius. This critical radius will likely be larger than the cross-over between the CH₄ and CO C I sources. If this cross-over occurs outside the *GALEX* FOV, it will have no effect on our measurements. If the cross-over occurs within the *GALEX* FOV, our estimate of the carbon ionization lifetime could be lowered by no more than 12% (the difference between the outflow velocities of carbon from CO and CH₃OH). This is well within the systematic uncertainty induced by our background subtraction (§3.1, Fig. 4, §4.2 and Table 3) and comparable to the uncertainty in our lifetime measurement caused by our choice of r_{\min} (§4.1).

It is also interesting to note that the CO lifetime may be shorter than 5×10^5 s (rate $> 2 \times 10^{-6} \text{ s}^{-1}$) and that C I emission from the CH₄ chain contributes less than we estimate. Using the solar maximum Tozzi et al. (1998) CO photodissociation rate value and the solar wind ionization rates from Rubin et al. (2009), the CO lifetime could be as short as 3.3×10^5 s ($3.0 \times 10^{-6} \text{ s}^{-1}$). When we make this change to our model we find that carbon production from CH₄ decreases to $1.0 \times 10^{28} \text{ s}^{-1}$ but that there is no change in the carbon production rate from CO. The production rate of carbon from CO could be lowered toward the $Q(\text{C})_{\max}$ value quoted in Table 5 if we included carbon from CH₃OH in our model. As we have shown in the previous paragraphs, these adjustments do not effect the ultimate goal of this work: the measurement of the carbon ionization lifetime. We look forward to continuing the analysis of our grism data to directly measure the CO lifetime and better constrain the production rates of the various carbon parent molecules with these UV data. Calculation of the excess energies of dissociation of CH₂ to solar photodissociation would also be useful in verifying our CH₄ chain analysis.

6. Conclusion

We have used high-quality FUV observations of comet C/2004 Q2 (Machholz) collected by the *GALEX* satellite and simple comet coma modeling techniques to measure the lifetime of ground state atomic carbon against ionization processes in interplanetary space. Scaled to 1 AU, we measure a value of $7.1 - 9.6 \times 10^5$ s (ionization rate of $1.0 - 1.4 \times 10^{-6}$ s $^{-1}$). This measurement compares favorably to calculations of the total ionization lifetime from three processes (in order of importance): solar wind proton charge exchange, solar photoionization, and solar wind electron impact ionization, assuming the comet was in the slow solar wind (Table 3).

Comet Machholz was observed at a heliographic latitude of 30° , which is near the boundary between the fast and slow solar wind (Bzowski et al. 2003). Our measurement was sensitive enough to determine that the comet was in the slow solar wind (§5 and Fig. 4). Together with ion tail observations, observation of the scale length of C I can therefore provide diagnostics of solar wind conditions at heliographic latitudes not often sampled by spacecraft.

The principal measurement uncertainty in the determination of the carbon ionization lifetime was related to the uncertainty in determining the background in the direct-mode comet image. The C I scale length was significantly larger than the FOV radius, so the background could not be determined *a priori* from the comet image itself. A background image recorded a month earlier was used, but, as first noted by Sujatha et al. (2009), variable airglow contamination makes simple-minded background subtraction of *GALEX* data recorded at different times highly inaccurate. We created a general method for the removal of airglow contamination that accurately considers observing geometry. This method could be improved using more physically accurate airglow emitter profiles from ionospheric and plasmaspheric models.

Our method of simultaneously using the *GALEX* direct and grism-mode observations has made it possible to measure the ionization lifetime of carbon and begin to probe the distribution of the various carbon parent molecules. With careful cleaning of background sources from the grism data, this work will continue. In particular, it will be possible to use our parameter optimizer to directly measure the CO lifetime. With the addition of optical depth effects to our *g*-factor calculations, we will also be able to use the *GALEX* data to determine if CO comes from a distributed source in comet Machholz.

GALEX has observed two other comets to date in the FUV: 8P/Tuttle and C/2007 N3 (Lulin) and six comets in the NUV: C/2004 Q2 (Machholz), 9P/Tempel 1, 73P/Schwassmann-Wachmann 3 Fragments B and C, 8P/Tuttle and C/2007 N3 (Lulin). The *GALEX* NUV channel includes emission from the bright OH 3080 Å band, the CS 2576 Å band, dust continuum and CO $^+$ features. The combined image and grism-mode analysis described here is also applicable to the *GALEX* NUV data.

We thank Karl Foster for his help planning the *GALEX* comet observations, Tim Conrow, and

the entire *GALEX* pipeline team for providing high quality products to work with, Jon Giorgini and the JPL HORIZONS team for calculating high quality cometary ephemerides from the perspective of *GALEX*, and Wayne Landsman and the many contributors to the IDLASTRO library. *GALEX* is operated for NASA by the California Institute of Technology under NASA contract NAS5-98034. This work was supported as part of the *GALEX* Guest Investigator program, grant NNG05GJ93G and NNX08AE14G to the University of Washington and NNX08AU56G to the Planetary Science Institute and NASA Planetary Atmospheres Grant NNX09AB59G to the University of Michigan. This is PSI Contribution Number 493.

Facilities: GALEX.

REFERENCES

- Axford, W. I. 1972, in Solar Wind, ed. C. P. Sonett, P. J. Coleman, & J. M. Wilcox, Vol. 308, NASA (Washington, D.C.: NASA Special Publication), 609
- Bockelée-Morvan, D., Boissier, J., Biver, N., & Crovisier, J. 2010, *Icarus*, 210, 898
- Bockelée-Morvan, D., Crovisier, J., Mumma, M. J., & Weaver, H. A. 2004, in Comets II, ed. M. C. Festou, H. U. Keller, & H. A. Weaver (Tucson, AZ: Univ. Arizona Press), 391
- Bonev, B. P., Mumma, M. J., Gibb, E. L., Di Santi, M. A., Villanueva, G. L., Magee-Sauer, K., & Ellis, R. S. 2009, *ApJ*, 699, 1563
- Brittnacher, M., et al. 2001, *Geophys. Res. Lett.*, 28, 2561
- Brooke, T. Y., Weaver, H. A., Chin, G., Bockelée-Morvan, D., Kim, S. J., & Xu, L.-H. 2003, *Icarus*, 166, 167
- Budzien, S. A., Festou, M. C., & Feldman, P. D. 1994, *Icarus*, 107, 164
- Bzowski, M., Mäkinen, T., Kyrölä, E., Summanen, T., & Quémerais, E. 2003, *A&A*, 408, 1165
- Combi, M. R., Cochran, A. L., Cochran, W. D., Lambert, D. L., & Johns-Krull, C. M. 1999, *ApJ*, 512, 961
- Combi, M. R., Harris, W. M., & Smyth, W. H. 2004, in Comets II, ed. M. C. Festou, H. U. Keller, & H. A. Weaver (Tucson, AZ: Univ. Arizona Press), 523
- Di Santi, M. A., Mumma, M. J., Dello Russo, N., & Magee-Sauer, K. 2001, *Icarus*, 153, 361
- Eberhardt, P., et al. 1987, *A&A*, 187, 481
- Feldman, P. D., Cochran, A. L., & Combi, M. R. 2004, in Comets II, ed. M. C. Festou, H. U. Keller, & H. A. Weaver (Tucson, AZ: Univ. Arizona Press), 425

- Feldman, P. D., Takacs, P. Z., Fastie, W. G., & Donn, B. 1974, *Science*, 185, 705
- Festou, M. C. 1981, *A&A*, 95, 69
- . 1984, *Adv. Space Res.*, 4, 165
- Glinski, R. J., Ford, B. J., Harris, W. M., Anderson, C. M., & Morgenthaler, J. P. 2004, *ApJ*, 608, 601
- Harris, W. M., Nordsieck, K. H., Scherb, F., & Mierkiewicz, E. J. 1999, *Earth, Moon, Planets*, 78, 161
- Harris, W. M., Scherb, F., Mierkiewicz, E. J., Oliverson, R. J., & Morgenthaler, J. P. 2002, *ApJ*, 578, 996
- Haser, L. 1957, *Bull. Soc. R. Sci. Liège*, 43, 740
- Hibbert, A., Biemont, E., Godefroid, M., & Vaeck, N. 1993, *A&AS*, 99, 179
- Huebner, W. F., Keady, J. J., & Lyon, S. P. 1992, *Astrophys. Space Sci.*, 195, 1
- Kobayashi, H., & Kawakita, H. 2009, *ApJ*, 703, 121
- Krishna-Swamy, K. S., & Brandt, J. C. 1986, *Nature*, 323, 404
- Kupperman, D. G. 1999, PhD thesis, The Johns Hopkins University
- Lupu, R. E., Feldman, P. D., Weaver, H. A., & Tozzi, G.-P. 2007, *ApJ*, 670, 1473
- Markwardt, C. B. 2009, in *ASP Conf. Ser.*, Vol. 411, *Astronomical Data Analysis Software and Systems XVIII*, ed. D. A. Bohlender, D. Durand, & P. Dowler (San Francisco, CA: ASP), 251
- Martin, D. C., et al. 2005, *ApJ*, 619, L1
- McPhate, J. B., Feldman, P. D., McCandliss, S. R., & Burgh, E. B. 1999, *ApJ*, 521, 920
- Meier, R., & A'Hearn, M. F. 1997, *Icarus*, 125, 164
- Moré, J. 1978, in *Lecture Notes in Mathematics*, Vol. 630, *Numerical Analysis*, ed. G. Watson (Berlin: Springer), 105
- Morrissey, P., et al. 2005, *ApJ*, 619, L7
- . 2007, *ApJS*, 173, 682
- Opal, C. B., Carruthers, G. R., Prinz, D. K., & Meier, R. R. 1974, *Science*, 185, 702
- Rubin, M., Hansen, K. C., Gombosi, T. I., Combi, M. R., Altwegg, K., & Balsiger, H. 2009, *Icarus*, 199, 505

- Smith, A. M., Stecher, T. P., & Casswell, L. 1980, *ApJ*, 242, 402
- Smith, E. J., & Marsden, R. G. 1995, *Geophys. Res. Lett.*, 22, 3297
- Sujatha, N. V., Murthy, J., Karnataki, A., Henry, R. C., & Bianchi, L. 2009, *ApJ*, 692, 1333
- Tozzi, G. P., Feldman, P. D., & Festou, M. C. 1998, *A&A*, 330, 753
- Tseng, W.-L., Bockelée-Morvan, D., Crovisier, J., Colom, P., & Ip, W.-H. 2007, *A&A*, 467, 729
- van Dishoeck, E. F., Beaerda, R. A., & van Hemert, M. C. 1996, *A&A*, 307, 645
- Whipple, F. L., & Huebner, W. F. 1976, *ARA&A*, 14, 143